

Learning spectrograms with convolutional spectral kernels

Zheyang Shen Markus Heinonen Samuel Kaski
Helsinki Institute for Information Technology, HIIT
Department of Computer Science, Aalto University

October 15, 2019

Abstract

We introduce the *convolutional spectral kernel* (CSK), a novel family of non-stationary, nonparametric covariance kernels for Gaussian process (GP) models, derived from the convolution between two imaginary radial basis functions. We present a principled framework to interpret CSK, as well as other deep probabilistic models, using approximated Fourier transform, yielding a concise representation of input-frequency *spectrogram*. Observing through the lens of the spectrogram, we provide insight on the interpretability of deep models. We then infer the functional hyperparameters using scalable variational and MCMC methods. On small- and medium-sized spatiotemporal datasets, we demonstrate improved generalization of GP models when equipped with CSK, and their capability to extract non-stationary periodic patterns.

1 Introduction

Gaussian processes (GP), as rich distributions over functions, are a cornerstone of a wide array of probabilistic modeling paradigms, thanks largely to their tractability, flexibility, robustness to overfitting and principled quantification of uncertainty (Rasmussen and Williams, 2006). At the helm of every GP model lies the *covariance kernel*, a function depicting its covariance structure and encoding prior knowledge.

Despite their equivalence to infinitely wide neural networks (Williams, 1997), GP models seldom exhibit the generalization of the former due to the innate rigidity of the commonly used squared exponential (SE) kernel, rendering them insufficient for genuine pattern recognition. While myriad studies (Paciorek and Schervish, 2004; Alvarez et al., 2009; Wilson and Adams, 2013; Duvenaud et al., 2013; Tobar et al., 2015; Wilson et al., 2016; Remes et al., 2017; Tobar,

2018; Shen et al., 2019) have sought more expressive kernel choices, their efforts fall notably short on (i) flexibility, (ii) interpretability or (iii) scalability, all of which are essential to large-scale statistical analysis. In this work, we propose and analyze a novel kernel family satisfying the above three properties.

We propose the *convolutional spectral kernel* (CSK), a novel kernel family with both spatially varying lengthscales and frequencies, derived from the convolution of two complex radial basis functions. We demonstrate that CSK possesses superior flexibility, unifying the monotonic non-stationary quadratic (NSQ) kernel (Paciorek and Schervish, 2004) and the stationary spectral mixture (SM) kernel (Wilson and Adams, 2013).

We introduce the notion of the *spectrogram* as a new, principled framework to interpret nonparametric kernels. The spectrogram is a joint distribution of input and frequency, conveniently displaying local covariance patterns. Our analysis shows that CSK retains an unbiased description of the instantaneous frequency, as opposed to the similar generalized spectral mixture (GSM) kernel (Remes et al., 2017). Meanwhile, our analysis sheds light on previously un-interpretable state-of-the-art deep probabilistic models, namely deep GPs (Damianou and Lawrence, 2013; Salimbeni and Deisenroth, 2017a; Havasi et al., 2018) and the deep kernel learning (Wilson et al., 2016), and justifies the adoption of certain heuristics in the said models.

We introduce scalable inference schemes for GP models equipped with CSK, which combine sparse GPs (Snelson and Ghahramani, 2006; Titsias, 2009; Hensman et al., 2017), stochastic gradient Hamiltonian Monte Carlo (Neal, 1993; Chen et al., 2014), and the recently proposed moving window MCEM (Havasi et al., 2018). Our method can be extended to covariance function deep GPs (Dunlop et al., 2018), a hierarchical generalization of our current model.

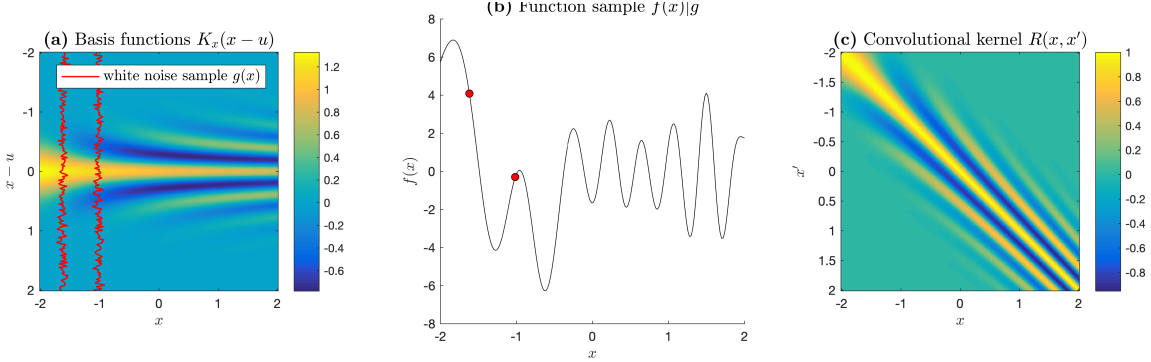


Figure 1: Visualization of the **(a)** basis function and convolution with a white noise process; **(b)** a sample from the resulting GP, where the highlighted points are computed from a convolution between the moving white noise process, denoted by the jagged lines in **(a)**; **(c)** the kernel matrix of the resulting CSK.

Lastly, we provide empirical evidence from both synthetic and real-world spatiotemporal datasets to support our theoretical claims. Our experiments visually and numerically demonstrate interpretable pattern extraction, along with superior predictive performance of the CSK-GP model.

2 Convolutional spectral kernel (CSK)

In this section, we derive the *convolutional spectral kernel*, a non-stationary, nonparametric kernel, interpretable through its local lengthscale, frequency and variance functions. Throughout the discussion of this paper, we assume a simple regression task: the objective is to infer a scalar function $f(\mathbf{x}) \in \mathbb{R}$ with D -dimensional inputs $\mathbf{x} \in \mathbb{R}^D$, with a finite supply of N observed data points as a data matrix $\mathbf{X} \in \mathbb{R}^{N \times D}$, and a set of noisy observations $\mathbf{y} \in \mathbb{R}^N$. We assume the function f is a realization of some underlying zero-mean Gaussian process, with homoskedastic observation noise of precision β ,

$$f(\mathbf{x}) \sim \mathcal{GP}(0, k(\mathbf{x}, \mathbf{x}')), \quad (1)$$

$$y = f(\mathbf{x}) + \epsilon, \quad \epsilon \sim \mathcal{N}(0, \beta^{-1}). \quad (2)$$

Our construction of CSK is inspired by the construction of non-stationary kernels with spatially-varying lengthscales (Gibbs, 1998; Higdon et al., 1998; Paciorek and Schervish, 2004). We propose a novel feature map $K_{\mathbf{x}}(\mathbf{u}) \in \mathbb{C}$ of complex-valued radial

bases:

$$K_{\mathbf{x}_i}(\mathbf{u}) = e^{-\frac{\|\Sigma_i^{-1/2}(\mathbf{u}-\mathbf{x}_i)\|^2}{2}} \exp(\iota(\Sigma_i^{-1}\boldsymbol{\mu}_i, \mathbf{u}-\mathbf{x}_i)) \propto \mathcal{N}(\mathbf{u}|\mathbf{x}_i + \iota\boldsymbol{\mu}_i, \Sigma_i). \quad (3)$$

Here we abuse the notation of a multivariate normal density, where ι denotes the imaginary unit, $\mathbf{u} \in \mathbb{R}^D$ denotes a point in input space, and the $\boldsymbol{\mu}_i := \boldsymbol{\mu}(\mathbf{x}_i) \in \mathbb{R}^D$, $\Sigma_i := \Sigma(\mathbf{x}_i) \in \mathbb{R}_{>0}^{D \times D}$ are vector- and positive-semidefinite matrix-valued functions of \mathbf{x}_i denoting the frequency and covariance parameters of the input space, from which we can construct the *frequency* as an inverse product $\Sigma^{-1}\boldsymbol{\mu}$. Viewing GPs as continuously-indexed moving average processes, the feature map (3) denotes a potentially infinite window (Tobar et al., 2015). We can henceforth represent a GP as a convolution between $K_{\mathbf{x}_i}$ and a white noise process $g(\mathbf{x}) \sim \mathcal{GP}(0, \delta_{\mathbf{x}=\mathbf{x}'})$ (Higdon et al., 1998):

$$f(\mathbf{x}_i) = \int K_{\mathbf{x}_i}(\mathbf{u})g(\mathbf{u}) \, d\mathbf{u}. \quad (4)$$

The kernel of f is the Hermitian inner product between $K_{\mathbf{x}_i}(\mathbf{u})$ and $K_{\mathbf{x}_j}(\mathbf{u})$, which is solved analytically:

$$k(\mathbf{x}_i, \mathbf{x}_j) = \int K_{\mathbf{x}_i}(\mathbf{u})\overline{K_{\mathbf{x}_j}(\mathbf{u})} \, d\mathbf{u} \propto \mathcal{N}(\mathbf{x}_i - \mathbf{x}_j|\iota(\boldsymbol{\mu}_i + \boldsymbol{\mu}_j), \Sigma_i + \Sigma_j). \quad (5)$$

Here $\overline{K_{\mathbf{x}_i}(\cdot)}$ denotes the complex conjugate. The solution to this integral is detailed in Section 1 of the appendix. We obtain a non-stationary correlation

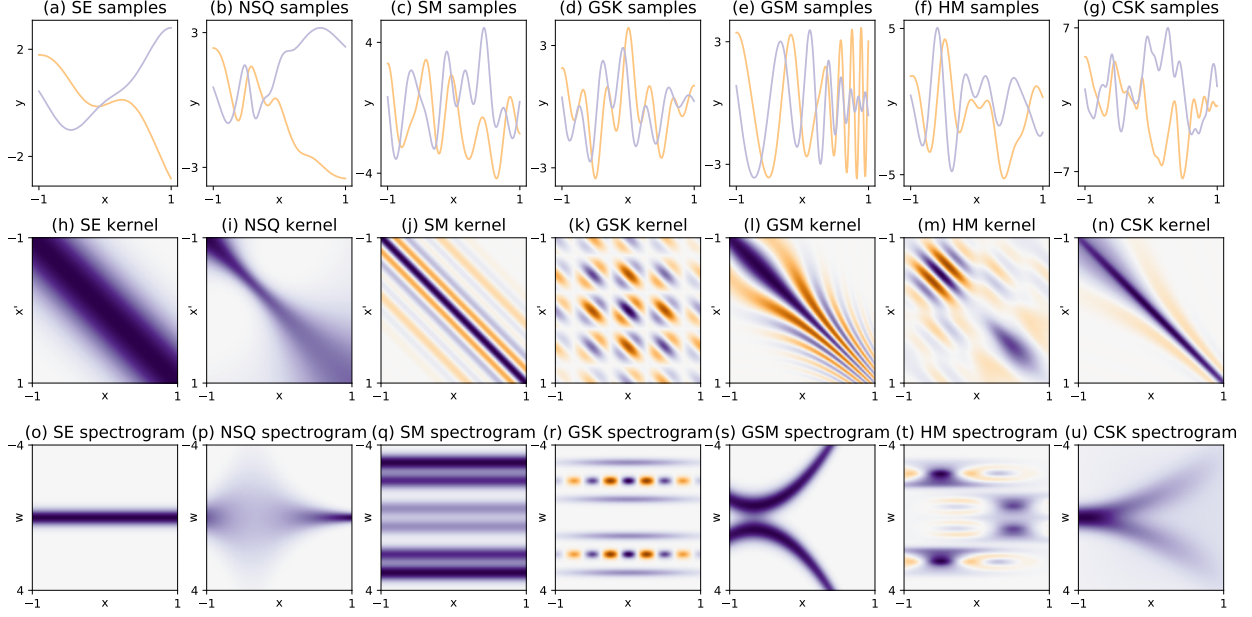


Figure 2: Overview of some kernels used in GP models, with sample paths (first row), kernel matrices (second row), and spectrogram (third row). Examples include SE (Rasmussen and Williams, 2006), NSQ (Paciorek and Schervish, 2004), SM (Wilson and Adams, 2013), GSK (Samo, 2017), GSM (Remes et al., 2017), HM (Shen et al., 2019) and CSK (current work).

function after normalization:

$$R(\mathbf{x}_i, \mathbf{x}_j) = \frac{\text{Re}(k(\mathbf{x}_i, \mathbf{x}_j))}{\sqrt{k(\mathbf{x}_i, \mathbf{x}_i)k(\mathbf{x}_j, \mathbf{x}_j)}} = \sigma_{ij} e^{-\frac{Q_{ij} + S_{ij}}{2}} \cos(\boldsymbol{\omega}_{ij}, \mathbf{x}_i - \mathbf{x}_j), \quad (6)$$

$$\sigma_{ij} = \frac{|\boldsymbol{\Sigma}_i|^{1/4} |\boldsymbol{\Sigma}_j|^{1/4}}{|\boldsymbol{\Sigma}_i + \boldsymbol{\Sigma}_j|^{1/2}}, \quad (7)$$

$$Q_{ij} = \left\| (\boldsymbol{\Sigma}_i + \boldsymbol{\Sigma}_j)^{-1/2} (\mathbf{x}_i - \mathbf{x}_j) \right\|^2, \quad (8)$$

$$\boldsymbol{\omega}_{ij} = (\boldsymbol{\Sigma}_i + \boldsymbol{\Sigma}_j)^{-1} (\boldsymbol{\mu}_i + \boldsymbol{\mu}_j), \quad (9)$$

$$S_{ij} = \left\| (\boldsymbol{\Sigma}_i^{-1} + \boldsymbol{\Sigma}_j^{-1})^{-1/2} (\boldsymbol{\omega}_{ii} - \boldsymbol{\omega}_{jj}) \right\|^2. \quad (10)$$

We can see from the cosine term in (6) that CSK computes *pairwise frequencies* $\boldsymbol{\omega}_{ij}$ for each pair of data points, and the exponential terms include squared Mahalanobis distances between \mathbf{x}_i and \mathbf{x}_j (8), and between local frequencies $\boldsymbol{\omega}_{ii}$ and $\boldsymbol{\omega}_{jj}$ (10).

CSK unifies two generalizations of the SE kernel. Paciorek and Schervish (2004) generalize the SE kernel by allowing lengthscales to spatially vary, which

is a special case of CSK when $\boldsymbol{\mu}_i \equiv \mathbf{0}$. Formally,

$$k_{NS}(\mathbf{x}_i, \mathbf{x}_j) = \sigma_{ij} e^{-\frac{Q_{ij}}{2}} \propto \mathcal{N}(\mathbf{x}_i | \mathbf{x}_j, \boldsymbol{\Sigma}_i + \boldsymbol{\Sigma}_j). \quad (11)$$

The spectral mixture kernel (Wilson and Adams, 2013) generalizes the SE kernel by allowing for non-zero frequency mean, which is a special case of CSK when functions $\boldsymbol{\mu}_i$ and $\boldsymbol{\Sigma}_i$ are kept constant:

$$k_{SM}(\mathbf{x}_i, \mathbf{x}_j) = k_{SE}(\mathbf{x}_i, \mathbf{x}_j) \cos(\boldsymbol{\mu}, \mathbf{x}_i - \mathbf{x}_j). \quad (12)$$

CSK as a correlation function identifies one frequency component in the underlying data, while the data might exhibit behaviors such as multiple frequencies and spatially varying variances. Such behaviors can be accounted for by stacking multiple CSKs multiplied by a standard deviation function $\sigma_p(\cdot) \in \mathbb{R}_{\geq 0}$:

$$k_{CS}(\mathbf{x}_i, \mathbf{x}_j) = \sum_{p=1}^P \sigma_p(\mathbf{x}_i) \sigma_p(\mathbf{x}_j) R_p(\mathbf{x}_i, \mathbf{x}_j). \quad (13)$$

CSK is defined through the component functions $\sigma_p(\cdot)$, $\boldsymbol{\Sigma}_p(\cdot)$, and $\boldsymbol{\mu}_p(\cdot)$. We denote the vector of functional parameters as $\boldsymbol{\theta}$, and each functional parameter $\theta_d(\mathbf{x})$

has a warped GP (Snelson et al., 2004) prior:

$$\theta_d(\mathbf{x}_i) = F_d(h_d(\mathbf{x}_i)), \quad (14)$$

$$h_d(\mathbf{x}_i) \sim \mathcal{GP}(0, k_d(\mathbf{x}_i, \mathbf{x}_j)), \quad (15)$$

For simplification, we assume diagonal covariances: $\Sigma_p = \text{diag}(\ell_{p1}^2, \dots, \ell_{pD}^2)$. The warping function F_d ensures the CSK to be positive definite.

3 The spectrogram

This section coins the notion of *spectrogram*, a joint input-frequency distribution, as a principled framework to interpret typical nonparametric kernels encountered in GP models, which typically lacks interpretability.

In signal processing and time-series analysis, the Wigner transform (Flandrin, 1998) converts covariance functions into quasi-probability distributions between input and frequency via a Fourier transform:

$$W(\mathbf{x}, \boldsymbol{\omega}) = \int_{\mathbb{R}^D} k\left(\mathbf{x} + \frac{\boldsymbol{\tau}}{2}, \mathbf{x} - \frac{\boldsymbol{\tau}}{2}\right) e^{-2i\pi\boldsymbol{\omega}^\top \boldsymbol{\tau}} d\boldsymbol{\tau}. \quad (16)$$

The Wigner distribution function (WDF) $W(\mathbf{x}, \boldsymbol{\omega})$ is a generalized probability distribution that retains instantaneous spectral density on all inputs. Despite their potential in interpretation, few machine learning models (Shen et al., 2019) apply the transform (16) due to its intractability.

In this work, we consider all kernels taking the form of a generalized mixture of Gaussian characteristic functions, as indexed by \mathcal{A} :

$$k(\mathbf{x}_i, \mathbf{x}_j) = \sum_{a \in \mathcal{A}} \sigma_{ij}^{(a)} e^{-\frac{D_{ij}^{(a)}}{2}} \exp(iU_{ij}). \quad (17)$$

Here the σ , D and U are real-valued functions of \mathbf{x}_i and \mathbf{x}_j . A linearized approximation of the above

functions gives an estimate of the kernel value, where the variables \mathbf{x} and $\boldsymbol{\tau}$ are separated:

$$k^{(a)}\left(\mathbf{x} + \frac{\boldsymbol{\tau}}{2}, \mathbf{x} - \frac{\boldsymbol{\tau}}{2}\right) \approx \sigma_{\mathbf{xx}}^{(a)} e^{-\frac{1}{2}\boldsymbol{\tau}^\top \Lambda_{\mathbf{x}}^{(a)} \boldsymbol{\tau}} \exp(i\langle \boldsymbol{\xi}_{\mathbf{x}}^{(a)}, \boldsymbol{\tau} \rangle), \quad (18)$$

$$\Lambda_{\mathbf{x}}^{(a)} = \mathcal{H}_{\mathbf{t}} D_{\mathbf{x}+\mathbf{t}/2, \mathbf{x}-\mathbf{t}/2} \Big|_{\mathbf{t}=\mathbf{0}}, \quad (19)$$

$$\boldsymbol{\xi}_{\mathbf{x}}^{(a)} = \mathcal{J}_{\mathbf{t}} U_{\mathbf{x}+\mathbf{t}/2, \mathbf{x}-\mathbf{t}/2} \Big|_{\mathbf{t}=\mathbf{0}}. \quad (20)$$

$\mathcal{H}_{\mathbf{t}}$ and $\mathcal{J}_{\mathbf{t}}$ in (19) and (20), respectively, denote the Hessian and Jacobian operators with respect to the variable \mathbf{t} . We can henceforth approximate the WDF with the kernel estimate (18):

$$\widehat{W}(\mathbf{x}, \boldsymbol{\omega}) = \sum_{a \in \mathcal{A}} \sigma_{\mathbf{xx}}^{(a)} \mathcal{N}\left(\boldsymbol{\omega} \left| \frac{\boldsymbol{\xi}_{\mathbf{x}}^{(a)}}{2\pi}, \frac{\Lambda_{\mathbf{x}}^{(a)}}{2\pi^2} \right.\right). \quad (21)$$

Our approximation is exact for both stationary and harmonizable spectral kernels (Wilson and Adams, 2013; Shen et al., 2019). The rest of the section delineates the significance of our method in interpreting CSK and deep GP (DGP) models. The models in interest and their spectrograms are listed in Table 1, and their derivation summarized in Section 2 of the appendix.

3.1 Spectrograms of non-stationary kernels

The spectrogram applies to GP models equipped with nonparametric kernels (Paciorek and Schervish, 2004; Damianou and Lawrence, 2013; Remes et al., 2017), as demonstrated in Table 1. In particular, we investigate the notable similarity between CSK and generalized spectral mixture (GSM) (Remes et al., 2017) kernel.

The GSM kernel is a nonparametric, quasi-periodic kernel with an intuitively defined spectrogram. The

Kernel	form	$\boldsymbol{\xi}_{\mathbf{x}}$	$\Lambda_{\mathbf{x}}$	reference
Spectral mixture	(12)	$\boldsymbol{\mu}$	Σ^{-1}	Wilson et al. (2015)
Non-stationary quadratic	(11)	$\mathbf{0}$	$\frac{1}{2}\Sigma_{\mathbf{x}}^{-1}$	Paciorek and Schervish (2004)
Generalized spectral mixture	(23)	$\boldsymbol{\mu}_{\mathbf{x}} + (\mathcal{J}_{\mathbf{x}}\boldsymbol{\mu}_{\mathbf{x}})\mathbf{x}$	$\frac{1}{2}\Sigma_{\mathbf{x}}^{-1}$	Remes et al. (2017)
Convolutional spectral kernel	(6)	$\Sigma_{\mathbf{x}}^{-1}\boldsymbol{\mu}_{\mathbf{x}}$	$\frac{1}{2}\left(\Sigma_{\mathbf{x}}^{-1} + \mathcal{J}_{\mathbf{x}}(\boldsymbol{\omega}_{\mathbf{xx}})^\top \Sigma_i \mathcal{J}_{\mathbf{x}}(\boldsymbol{\omega}_{\mathbf{xx}})\right)$	current work
DGP-SE	(26)	$\mathbf{0}$	$\mathcal{J}_{\mathbf{x}}\mathbf{f}_{L-1}^\top \Sigma^{-1} \mathcal{J}_{\mathbf{x}}\mathbf{f}_{L-1}$	Damianou and Lawrence (2013)

Table 1: Spectrogram function parameters for various non-stationary covariance function and compositional DGP.

correlation of GSM is a parametrization of (17)

$$D_{ij} = \left\| (\boldsymbol{\Sigma}_i + \boldsymbol{\Sigma}_j)^{-1/2} (\mathbf{x}_i - \mathbf{x}_j) \right\|^2, \quad (22)$$

$$U_{ij} = \langle \boldsymbol{\mu}_i, \mathbf{x}_i \rangle - \langle \boldsymbol{\mu}_j, \mathbf{x}_j \rangle. \quad (23)$$

While it is tempting to equate the frequency mean $\boldsymbol{\xi}_x$ (20) with $\boldsymbol{\mu}_i$, our analysis yields contradictory evidence, with $\boldsymbol{\xi}_{\mathbf{x}_i} = \boldsymbol{\mu}_i + (\mathcal{J}_x \boldsymbol{\mu})|_{\mathbf{x}=\mathbf{x}_i} \mathbf{x}_i$, rendering the GSM kernel inherently biased in instantaneous frequency, which leads to an erroneously defined intuitive spectrogram (Remes et al., 2017).

The CSK records unbiased frequencies in contrast, albeit suffers a bias in the lengthscales (as shown in Table 1). We posit that it is essential that we adopt unbiased frequencies, so that the kernel extracts correct periodicities.

3.2 Standard DGPs are equivalent to GPs with NSQ kernels

Through spectrogram analysis, we uncover an equivalence between two classes of DGPs, namely the ones constructed with compositions and the ones with nonparametric covariance functions (Dunlop et al., 2018).

The compositional DGP (Damianou and Lawrence, 2013; Salimbeni and Deisenroth, 2017a; Dunlop et al., 2018) generalizes standard GP with recursive functional composition:

$$f = f_L \circ f_{L-1} \circ \dots \circ f_0, \quad (24)$$

$$f_l \sim \mathcal{GP}(m_l, k_l), \quad l = 0, \dots, L. \quad (25)$$

The conditional kernel $k_l|f_{l-1}$ can be seen as one with varying lengthscales when k_L is the default SE kernel:

$$k_l(x, x'|f_{l-1}) = w^2 e^{-\frac{(f_{l-1}(x) - f_{l-1}(x'))^2}{2\ell^2}} \quad (26)$$

$$\approx w^2 \sigma_{ij} e^{-\frac{Q_{x,x'}}{2}} = k_{NS}(x, x'|\Sigma_i), \quad (27)$$

$$\Sigma_i = \frac{2\ell^2}{f_{l-1}'^2(x_i)}. \quad (28)$$

Here the $Q_{x,x'}$ corresponds to the squared distance defined in (8). According to our analysis (Table 1), the DGP kernel (26) and an NSQ kernel (11) with a lengthscale parametrization (28) share the same spectrogram, demonstrating an equivalence up to second-order effects.

3.3 Advantages of covariance function DGPs

Given the equivalence drawn in 3.2, we delineate the pros and cons between compositional DGPs and DGPs formulated with covariance functions (Dunlop et al., 2018), which comprise a layered structure of nonparametric kernels k_θ :

$$f_0(x) \sim \mathcal{GP}(0, k_\theta(x, x'|\theta = \theta_0)), \quad (29)$$

$$f_l(x)|f_{l-1}(x) \sim \mathcal{GP}(0, k_\theta(x, x'|\theta = F \circ f_{l-1})). \quad (30)$$

Here k_θ denotes such nonparametric kernels as NSQ (11) (Paciorek and Schervish, 2004), θ their functional hyperparameters, and F a warping function (14) mapping GP samples to valid parameters. Despite the notable equivalence, the two types of GP models behave differently in practice (Dunlop et al., 2018). This discrepancy warrants a closer investigation, which evidences the superiority of covariance function DGPs.

We posit that the deep compositional probabilistic models (24) could benefit from monotonicity in hidden layers f_0, f_1, \dots, f_{L-1} , a constraint not required for covariance function DGPs (30). Zero-mean compositional DGPs exhibit a pathology where the prior space of $f_L \circ \dots \circ f_0$ degenerates into piecewise constant functions as $L \rightarrow \infty$ (Duvenaud et al., 2014; Dunlop et al., 2018). The state-of-the-art DGPs (Salimbeni and Deisenroth, 2017a; Havasi et al., 2018) remedy this pathology with calibrated mean functions, which are likely to generate monotonic sample paths, despite the seemingly detrimental effect on model expressivity. Our derivation of approximate equivalence holds when the function $f_{l-1}(x)$ has nonzero derivatives almost everywhere, and is consequently monotonic. The ‘‘equivalence conditioned on monotonicity’’ marks the absence of rank pathology in covariance function DGPs (30) and provides alternate justification on calibrated mean functions.

Covariance function DGP avoids multi-modality by directly modeling lengthscales values. It is worth noting that the conditional kernel (26) stays invariant under *translation* and *reflection* of f_{l-1} , thus defining an equivalence class containing the above transformations. The invariance yields highly multi-modal posterior distributions (Havasi et al., 2018), a major obstacle to effective inference. The linear mean function (Salimbeni and Deisenroth, 2017a) solves reflection but not translation of f_{l-1} . Meanwhile, functions belonging to the same equivalence class correspond to a singular lengthscales (28), and consequently a single covariance function DGP, which has

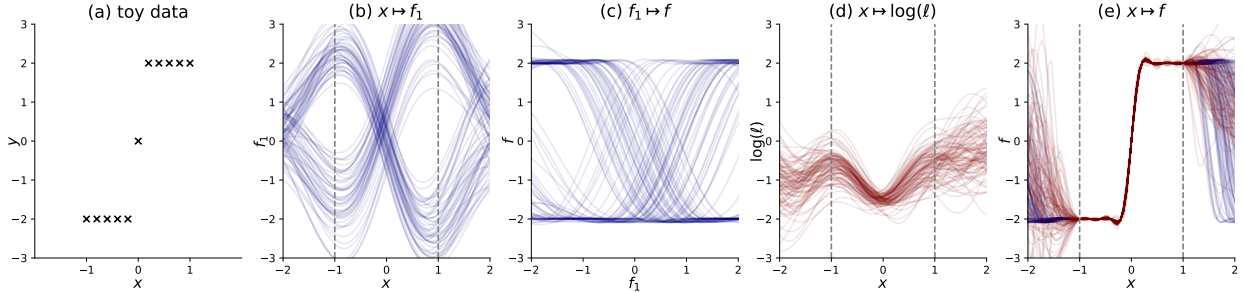


Figure 3: Posterior HMC draws on two DGPs. (b) and (c) demonstrate functions that are translations or mirror images of each other, while the multi-modal behavior disappears in (d).

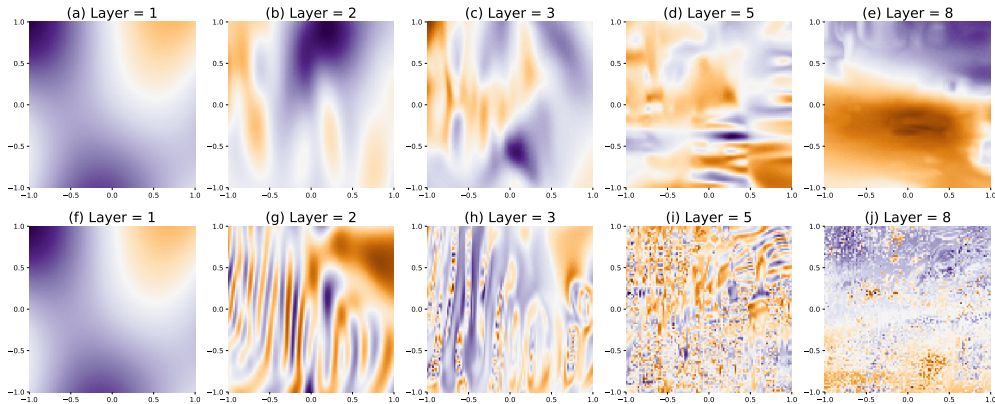


Figure 4: 2D prior draws from covariance function DGPs with correlation function NSQ (first row) and CSK (6) (second row).

notably more concentrated posterior densities. We demonstrate the two posteriors of a toy example in Figure 3.

While the covariance function DGP appears to claim a minor turf (Paciorek and Schervish, 2004; Heinonen et al., 2016; Remes et al., 2017) in deep probabilistic modeling, we advocate that it replace the customary compositional DGPs as an equivalent but more effective alternative.

3.4 CSK as deep Gaussian processes

Applying CSK (13) in the covariance function DGP recursion (30) yields a DGP that nests the NSQ construction (Dunlop et al., 2018) as a special case, defining a proven *ergodic* Markov chain (Dunlop et al., 2018). While the ergodicity of the DGP-CSK model upper bounds the model complexity with its mixing time, the application of CSK, nevertheless, significantly enriches the prior space (Figure 4).

4 Scalable inference for covariance function DGPs

In this section, we discuss the understudied scalable inference schemes for covariance function DGPs (Dunlop et al., 2018). Our inference framework places inducing points on functional kernel parameters θ and the function f . It shares the same time complexity as inducing point sparse DGPs (Salimbeni and Deisenroth, 2017a; Havasi et al., 2018). Consider a nonparametric kernel $k_\theta(\cdot, \cdot)$, where the functional hyperparameters θ have warped GP priors (14). Possible candidates of kernels include the NSQ kernel (11), GSM kernel (23) and CSK (13). Without loss of generality, we assume a 2-layer deep GP ($L = 1$):

$$f \sim \mathcal{GP}(0, k_\theta(\cdot, \cdot)), \quad (31)$$

$$\theta_d(\mathbf{x}) = F_d(h_d(\mathbf{x})), h_d(\mathbf{x}) \sim \mathcal{GP}(0, k_d(\cdot, \cdot)). \quad (32)$$

With noisy observations $\{\mathbf{X}, \mathbf{y}\}$ (2), inducing points $\mathbf{z}_f, \mathbf{z}_\theta$ and their respective observations $\mathbf{u}_f, \mathbf{u}_\theta$, we

can factorize the joint likelihood:

$$p(\mathbf{y}, \mathbf{f}, \boldsymbol{\theta}, \mathbf{u}) = \underbrace{p(\mathbf{y}|\mathbf{f})}_{\text{likelihood}} \underbrace{p(\mathbf{f}|\mathbf{u}_f, \boldsymbol{\theta})p(\mathbf{u}_f|\boldsymbol{\theta})p(\boldsymbol{\theta}|\mathbf{u}_\theta)p(\mathbf{u}_\theta)}_{\text{prior}}, \quad (33)$$

where $\boldsymbol{\theta} = \boldsymbol{\theta}(\mathbf{X} \cup \mathbf{z}_f)$. The posterior distribution $p(\mathbf{u}_\theta, \mathbf{u}_f|\mathbf{y})$ is intractable, and we approximate it with stochastic gradient Hamiltonian Monte Carlo (SG-HMC) (Chen et al., 2014; Havasi et al., 2018) and doubly stochastic variational inference (DS-VI) (Salimbeni and Deisenroth, 2017a). While we use 2-layer DGP as an example, the likelihood factorizes analogously for more layers.

4.1 Stochastic gradient Hamiltonian Monte Carlo

Hamiltonian Monte Carlo (HMC) (Neal, 1993) produces samples from the posterior distribution $p(\mathbf{u}|\mathbf{y})$, which requires the gradient computation for the negative log-posterior $U(\mathbf{u}) = -\log p(\mathbf{u}|\mathbf{y})$. SG-HMC (Chen et al., 2014) scales up classical HMC with stochastic gradient estimates.

Using Jensen’s inequality, we can observe from (33) that the lower bound of the joint log-likelihood $p(\mathbf{u}_\theta, \mathbf{u}_f, \mathbf{y})$ can be approximated via Monte Carlo sampling:

$$\begin{aligned} \log p(\mathbf{u}_\theta, \mathbf{u}_f, \mathbf{y}) &\geq \mathbb{E}_{p(\mathbf{f}|\mathbf{u}_f, \boldsymbol{\theta})p(\boldsymbol{\theta}|\mathbf{u}_\theta)} \log \frac{p(\mathbf{y}, \mathbf{f}, \boldsymbol{\theta}, \mathbf{u})}{p(\mathbf{f}|\mathbf{u}_f, \boldsymbol{\theta})p(\boldsymbol{\theta}|\mathbf{u}_\theta)} \\ &\approx \log p(\mathbf{y}|\hat{\mathbf{f}})p(\mathbf{u}_f|\hat{\boldsymbol{\theta}})p(\mathbf{u}_\theta). \end{aligned} \quad (34)$$

The vectors $\hat{\boldsymbol{\theta}}, \hat{\mathbf{f}}$ are Monte Carlo samples: $\hat{\boldsymbol{\theta}} \sim p(\boldsymbol{\theta}|\mathbf{u}_\theta), \hat{\mathbf{f}} \sim p(\mathbf{f}|\mathbf{u}_f, \hat{\boldsymbol{\theta}})$. We can thus approximate

the gradient using (34), where

$$\nabla U(\mathbf{u}_\theta, \mathbf{u}_f) = -\nabla \log p(\mathbf{u}_\theta, \mathbf{u}_f|\mathbf{y}) = -\nabla \log p(\mathbf{u}_\theta, \mathbf{u}_f, \mathbf{y}). \quad (35)$$

We refer to Section 3 in the appendix for hyperparameter training and stochastic variational inference for this model.

5 Experiments

5.1 Recovering chirp signal

We first tested our methods on a simulated dataset. A chirp signal is a non-stationary signal taking the generic form $x(t) = \cos(\phi(t))$. In this setting, we take 400 noisy observations of a chirp signal $x(t) = \cos(2\pi(t + 0.6t^3))$, and train a one-component CSK with 30 inducing points. The synthetic instantaneous frequency of this signal is $\phi'(t)/2\pi = 1 + 1.8t^2$, which is recovered with the frequency term in CSK (see figure 5).

5.2 Solar irradiance

We consider regression on the solar irradiance dataset (Lean, 2004), which has shown some non-stationarities. We compared GP models with NSQ, SM, HMK (Shen et al., 2019) and CSK, where the inference for SM and HMK were done with sparse GP regression with inducing points (Titsias, 2009), and the functional hyperparameters of NSQ and CSK are inferred with SGHMC as illustrated in the previous section. While it is not immediately clear from the spectrogram visualizations (see figure 6, the spectral kernels (SM, HMK and CSK) learns similar frequency patterns: SM learns global frequency peaks exhibited in data;

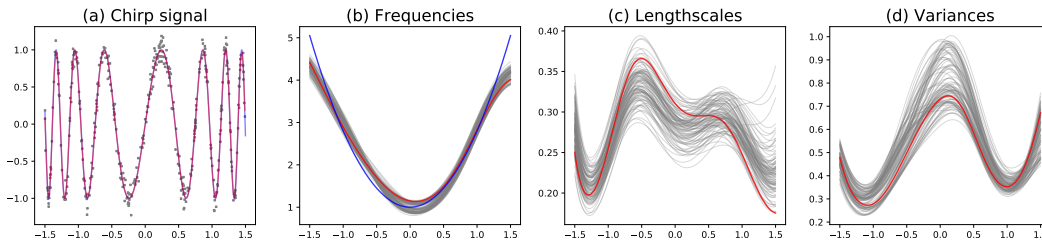


Figure 5: Regression on synthetic chirp signal. (a): The training data (grey points) with the ground truth line (blue) and predicted mean (red); ground truth and predict mean overlap. (b): HMC samples of the learned frequency function, with ground truth instantaneous frequency (blue line) and MAP estimate (red line). (c), (d): HMC samples of lengthscale and variance functions, with MAP estimates marked with red lines.

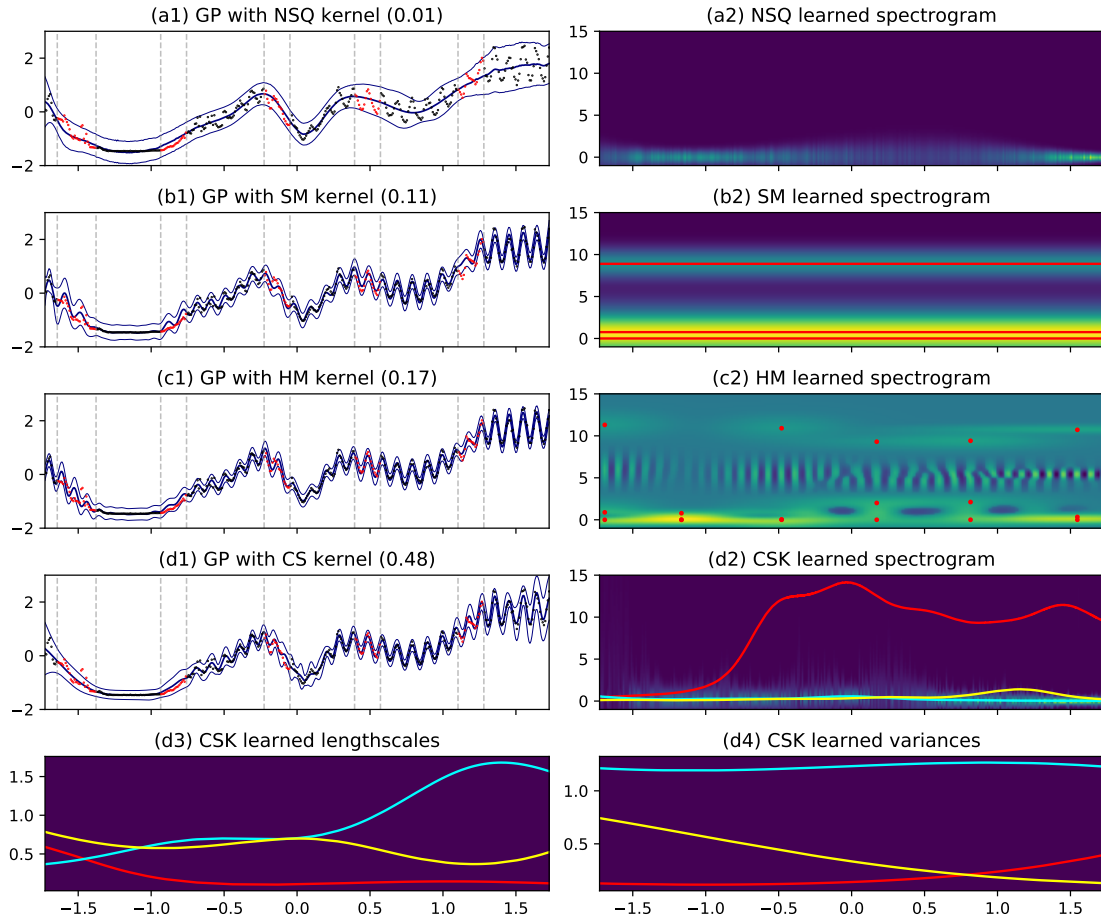


Figure 6: GP regression with solar irradiance. Test log-likelihoods are shown in parentheses for figures (a1)-(d1). The learned frequencies are marked by the red lines and points on the spectrogram plot (b2)-(d2). The lengthscale and variance function learned from CSK is plotted on (d3)-(d4).

HMK learns and interpolates local patterns; CSK learns a global pattern with varying frequencies, while also accounting for the non-Gaussianity of the data.

5.3 Air temperature anomaly dataset

We conducted spatiotemporal analysis on the air temperature anomaly dataset (Jones, 1994), which contains monthly air temperature deviations from the monthly mean temperature measured on locations on a global grid. We subsampled the data from 1988-1993 with 32910 readings and partitioned an 80%-20% split on training and testing data. Figure 7 demonstrates the predictive temperature anomaly between a GP with SE kernel and CSK with 5 components, which significantly improves the predictive performance. Nonstationarity is required to capture

the correlation patterns demonstrated in the data.

5.4 New York Yellow Taxi dataset

We ran GP regression on a subset of the New York Yellow Taxi dataset¹, whose objective is to predict the taxi trip duration given the pickup and dropoff locations and the starting date and time. Given CSK’s ability to handle periodicities, we treat the date and time as one feature. We ran 7 different models in total: Bayesian linear regression (LINEAR), vanilla sparse GPs with 100 and 500 inducing points (VANILLA 100 & 500), sparse GP with SM kernel (SM), 4-layer compositional deep GP with “mono-

¹http://www.nyc.gov/html/tlc/html/about/trip_record_data.shtml

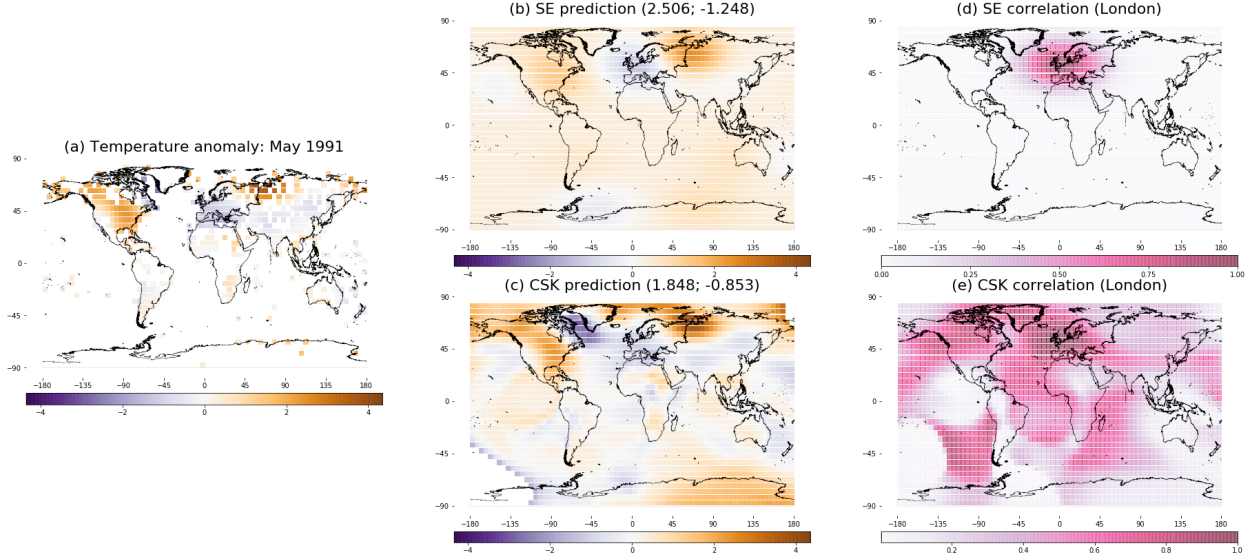


Figure 7: Air temperature anomaly dataset. (a) demonstrates the temperature anomaly readings from May 1991. (b), (c) display the posterior predictive mean for May 1991 on a grid of global locations, with the numbers in parentheses denoting mean squared error (MSE) and mean log-likelihood, respectively. (d), (e) depict the correlation between London and other geographical locations: it is worth noting that the SE kernel (d) only captures positive correlation on a small elliptical region.

Model	LINEAR	VANILLA 100	VANILLA 500	SM	DGP 4	NSQ	CSK
Test log-likelihood	-1.278	-0.847	-0.823	-0.805	-0.623	-0.580	-0.576
Test MSE	0.755	0.333	0.314	0.298	0.303	0.293	0.289

Table 2: GP regression results for NY taxi dataset.

tonic” inner layers (DGP 4), GP with NSQ and CSK. Apart from VANILLA 500, other models were run with 100 inducing points.

One can tell from comparison in Table 2 that the taxi dataset is nonlinear, non-Gaussian and exhibits nontrivial frequency patterns. CSK marginally outperforms better than other model by accounting for all three properties. NSQ outperforms a 4-layer DGP due to a different parametrization: NSQ is roughly equivalent to a 2-layer DGP where the inner layers for each data dimensions are modelled with SE kernels with independent lengthscales.

6 Conclusion

In this work, we propose the *convolutional spectral kernel*, which generalizes Paciorek and Schervish (2004) with spatially varying frequencies. We analyze common kernels and GP models having input warping with spectrogram, which sheds light on the

interpretation of deep models, and draws an equivalence between two types of DGPs. We propose a novel scalable inference framework for DGPs constructed via covariance functions, which empirically outperforms current compositional DGP methods. The theoretical results derived in this paper indicate that covariance function DGPs, as an appealing alternative to current DGPs, warrant further study.

References

- M. Alvarez, D. Luengo, and N. D. Lawrence. Latent force models. In *Artificial Intelligence and Statistics*, pages 9–16, 2009.
- T. Chen, E. Fox, and C. Guestrin. Stochastic gradient Hamiltonian Monte Carlo. In *International Conference on Machine Learning*, pages 1683–1691, 2014.
- A. Damianou and N. D. Lawrence. Deep Gaussian

- processes. In *Artificial Intelligence and Statistics*, pages 207–215, 2013.
- M. M. Dunlop, M. A. Girolami, A. M. Stuart, and A. L. Teckentrup. How deep are deep Gaussian processes? *The Journal of Machine Learning Research*, 19(1):2100–2145, 2018.
- D. Duvenaud, J. R. Lloyd, R. Grosse, J. B. Tenenbaum, and Z. Ghahramani. Structure discovery in nonparametric regression through compositional kernel search. In *International Conference on Machine Learning*, pages 1166–1174, 2013.
- D. Duvenaud, O. Rippel, R. Adams, and Z. Ghahramani. Avoiding pathologies in very deep networks. In *Artificial Intelligence and Statistics*, pages 202–210, 2014.
- P. Flandrin. *Time-frequency/time-scale analysis*, volume 10. Academic press, 1998.
- Y. Gal and R. Turner. Improving the Gaussian process sparse spectrum approximation by representing uncertainty in frequency inputs. In *International Conference on Machine Learning*, pages 655–664, 2015.
- M. N. Gibbs. *Bayesian Gaussian processes for regression and classification*. PhD thesis, Citeseer, 1998.
- M. Havasi, J. M. Hernández-Lobato, and J. J. Murillo-Fuentes. Inference in deep Gaussian processes using stochastic gradient Hamiltonian Monte Carlo. In *Advances in Neural Information Processing Systems*, pages 7517–7527, 2018.
- M. Heinonen, H. Mannerström, J. Rousu, S. Kaski, and H. Lähdesmäki. Non-stationary Gaussian process regression with Hamiltonian Monte Carlo. In *Artificial Intelligence and Statistics*, pages 732–740, 2016.
- J. Hensman, N. Fusi, and N. D. Lawrence. Gaussian processes for big data. In *Proceedings of the Twenty-Ninth Conference on Uncertainty in Artificial Intelligence, UAI 2013, Bellevue, WA, USA, August 11-15, 2013*, 2013.
- J. Hensman, N. Durrande, and A. Solin. Variational fourier features for Gaussian processes. *Journal of Machine Learning Research*, 18:151–1, 2017.
- D. Higdon, J. Swall, and J. Kern. Non-stationary spatial modeling. *Bayesian Statistics*, 6, 1998.
- P. D. Jones. Hemispheric surface air temperature variations: a reanalysis and an update to 1993. *Journal of Climate*, 7(11):1794–1802, 1994.
- J. Lean. Solar irradiance reconstruction. *IGBP PAGES/World Data Center for Paleoclimatology Data Contribution Series*, 35, 2004.
- R. M. Neal. Probabilistic inference using Markov Chain Monte Carlo methods. Technical report, University of Toronto, 1993.
- C. J. Paciorek and M. J. Schervish. Nonstationary covariance functions for Gaussian process regression. In *Advances in Neural Information Processing Systems*, pages 273–280, 2004.
- C. E. Rasmussen and C. K. I. Williams. *Gaussian Processes for Machine Learning*. Adaptive Computation and Machine Learning. MIT Press, Cambridge, MA, USA, January 2006.
- S. Remes, M. Heinonen, and S. Kaski. Non-stationary spectral kernels. In *Advances in Neural Information Processing Systems*, pages 4642–4651, 2017.
- H. Salimbeni and M. Deisenroth. Doubly stochastic variational inference for deep Gaussian processes. In *Advances in Neural Information Processing Systems*, pages 4588–4599, 2017a.
- H. Salimbeni and M. P. Deisenroth. Deeply non-stationary Gaussian processes. In *Bayesian Deep Learning workshop, Advances in Neural Information Processing Systems*, 2017b.
- Y.-L. K. Samo. *Advances in kernel methods: towards general-purpose and scalable models*. PhD thesis, University of Oxford, 2017.
- Z. Shen, M. Heinonen, and S. Kaski. Harmonizable mixture kernels with variational Fourier features. In *Artificial Intelligence and Statistics*, pages 3273–3282, 2019.
- E. Snelson and Z. Ghahramani. Sparse Gaussian processes using pseudo-inputs. In *Advances in neural information processing systems*, pages 1257–1264, 2006.
- E. Snelson, Z. Ghahramani, and C. E. Rasmussen. Warped Gaussian processes. In *Advances in neural information processing systems*, pages 337–344, 2004.

- J. T. Springenberg, A. Klein, S. Falkner, and F. Hutter. Bayesian optimization with robust Bayesian neural networks. In *Advances in Neural Information Processing Systems*, pages 4134–4142, 2016.
- M. Titsias. Variational learning of inducing variables in sparse Gaussian processes. In *Artificial Intelligence and Statistics*, pages 567–574, 2009.
- F. Tobar. Bayesian nonparametric spectral estimation. In *Advances in Neural Information Processing Systems*, pages 10127–10137, 2018.
- F. Tobar, T. D. Bui, and R. E. Turner. Learning stationary time series using Gaussian processes with nonparametric kernels. In *Advances in Neural Information Processing Systems*, pages 3501–3509, 2015.
- C. K. I. Williams. Computing with infinite networks. In *Advances in Neural Information Processing Systems*, pages 295–301, 1997.
- A. G. Wilson and R. Adams. Gaussian process kernels for pattern discovery and extrapolation. In *International Conference on Machine Learning*, pages 1067–1075, 2013.
- A. G. Wilson, Z. Hu, R. Salakhutdinov, and E. P. Xing. Deep kernel learning. In *Artificial Intelligence and Statistics*, pages 370–378, 2016.
- Andrew G Wilson, Christoph Dann, Chris Lucas, and Eric P Xing. The human kernel. In *Advances in neural information processing systems*, pages 2854–2862, 2015.

Supplementary materials

1 Convolutional spectral kernels: a derivation

In this section, we derive the convolutional spectral kernel (CSK) in detail, which solves the following integral:

$$K_{\mathbf{x}_i}(\mathbf{x}_i - \mathbf{u}) = \mathcal{N}(\mathbf{x}_i - \mathbf{u} | \imath \boldsymbol{\mu}_i, \boldsymbol{\Sigma}_i) = \frac{1}{|2\pi \boldsymbol{\Sigma}_i|^{1/2}} \exp\left(-\frac{1}{2}(\mathbf{x}_i - \mathbf{u} - \imath \boldsymbol{\mu}_i)^\top \boldsymbol{\Sigma}_i^{-1}(\mathbf{x}_i - \mathbf{u} - \imath \boldsymbol{\mu}_i)\right), \quad (36)$$

$$k(\mathbf{x}_i, \mathbf{x}_j) = \int K_{\mathbf{x}_i}(\mathbf{x}_i - \mathbf{u}) \overline{K_{\mathbf{x}_j}(\mathbf{x}_j - \mathbf{u})} d\mathbf{u}. \quad (37)$$

Note that a transpose instead of Hermitian is used in the feature representation, making the function $K_{\mathbf{x}_i}(\mathbf{x}_i - \mathbf{u})$ an improper density. We denote the Fourier transform as an operator on functions: $\mathcal{F}[f](\boldsymbol{\omega}) = \int f(\mathbf{x}) e^{i\boldsymbol{\omega}^\top \mathbf{x}} d\mathbf{x}$. The Fourier transform of $K_{\mathbf{x}_i}(\mathbf{u})$ takes a simple form, which can be used to formulate the Fourier transform of the kernel:

$$\mathcal{F}[\mathcal{N}(\mathbf{v} | \imath \boldsymbol{\mu}, \boldsymbol{\Sigma})] = \exp\left(-\frac{1}{2}\boldsymbol{\omega}^\top \boldsymbol{\Sigma} \boldsymbol{\omega} - \boldsymbol{\mu}^\top \boldsymbol{\omega}\right), \quad (38)$$

$$k(\mathbf{x}_i - \mathbf{x}_j) = \mathcal{F}^{-1}\{\mathcal{F}[k(\mathbf{x}_i - \mathbf{x}_j)]\} \quad (39)$$

$$= \mathcal{F}^{-1}\left\{\mathcal{F}\left[\int K_{\mathbf{x}_i}(\mathbf{x}_i - \mathbf{u}) \overline{K_{\mathbf{x}_j}(\mathbf{x}_j - \mathbf{u})} d\mathbf{u}\right]\right\} \quad (40)$$

$$= \mathcal{F}^{-1}\left\{\mathcal{F}[K_{\mathbf{x}_i}(\mathbf{x}_i - \mathbf{u})] \mathcal{F}[\overline{K_{\mathbf{x}_j}(\mathbf{x}_j - \mathbf{u})}]\right\} \quad (41)$$

$$= \mathcal{F}^{-1}\left\{\mathcal{F}[K_{\mathbf{x}_i}(\mathbf{x}_i - \mathbf{u})] \overline{\mathcal{F}[K_{\mathbf{x}_j}(\mathbf{x}_j - \mathbf{u})]}\right\} \quad (42)$$

$$= \mathcal{F}^{-1}\left\{\mathcal{F}[K_{\mathbf{x}_i}(\mathbf{x}_i - \mathbf{u})] \mathcal{F}[K_{\mathbf{x}_j}(\mathbf{x}_j - \mathbf{u})]\right\} \quad (43)$$

$$= \mathcal{F}^{-1}\left\{\exp\left(-\frac{1}{2}\boldsymbol{\omega}^\top \boldsymbol{\Sigma}_i \boldsymbol{\omega} - \boldsymbol{\mu}_i^\top \boldsymbol{\omega} - \frac{1}{2}\boldsymbol{\omega}^\top \boldsymbol{\Sigma}_j \boldsymbol{\omega} - \boldsymbol{\mu}_j^\top \boldsymbol{\omega}\right)\right\} \quad (44)$$

$$= \mathcal{F}^{-1}\left\{\exp\left(-\frac{1}{2}\boldsymbol{\omega}^\top (\boldsymbol{\Sigma}_i + \boldsymbol{\Sigma}_j) \boldsymbol{\omega} - (\boldsymbol{\mu}_i + \boldsymbol{\mu}_j)^\top \boldsymbol{\omega}\right)\right\} \quad (45)$$

$$= \mathcal{N}(\mathbf{x}_i - \mathbf{x}_j | \imath(\boldsymbol{\mu}_i + \boldsymbol{\mu}_j), \boldsymbol{\Sigma}_i + \boldsymbol{\Sigma}_j). \quad (46)$$

The pseudo-Gaussian density gives a convenient closed-form Fourier transform, which we use to obtain the solution to the Hermitian inner product.

2 The spectrogram derivations

Many kernels share the form of a mixture of generalized Gaussian characteristic functions (CFs). In this section, we address certain qualities of the Gaussian characteristic functions that justify our approximation of the kernel. Consider the CF of a Gaussian distribution (spectral mixture kernel (Wilson and Adams, 2013)) the following generalized Gaussian CF:

$$k_{SM}(\mathbf{x}_i, \mathbf{x}_j) = \sigma \exp\left(-\frac{1}{2}(\mathbf{x}_i - \mathbf{x}_j)^\top \boldsymbol{\Sigma}^{-1}(\mathbf{x}_i - \mathbf{x}_j) + \imath \langle \boldsymbol{\mu}, \mathbf{x}_i - \mathbf{x}_j \rangle\right), \quad (47)$$

$$k(\mathbf{x}_i, \mathbf{x}_j) = \sigma_{ij} \exp\left(-\frac{1}{2}D_{ij} + \imath U_{ij}\right). \quad (48)$$

The Wigner transform is tractable for the SM kernel (47), because D_{ij} and U_{ij} terms are linearized with respect to $\boldsymbol{\tau} = \mathbf{x}_i - \mathbf{x}_j = (\mathbf{x} + \boldsymbol{\tau}/2) - (\mathbf{x} - \boldsymbol{\tau}/2)$. We can similarly linearize the two terms for an approximation

of kernel values, and get an approximate Wigner transform. Given by the property of a Gaussian CF, we give the following assumptions based on the convexity of D_{ij} and the zero diagonal of U_{ii} for k_{SM} .

$$D_{\mathbf{x},\mathbf{x}} = 0, \quad (49)$$

$$\mathcal{J}_{\mathbf{t}} D_{\mathbf{x}+\mathbf{t}/2,\mathbf{x}-\mathbf{t}/2} = \mathbf{0}, \quad (50)$$

$$\mathcal{H}_{\mathbf{t}} D_{\mathbf{x}+\mathbf{t}/2,\mathbf{x}-\mathbf{t}/2} \succeq \mathbf{0}, \quad (51)$$

$$U_{\mathbf{x},\mathbf{x}} = 0. \quad (52)$$

We approximate a Taylor expansion based on those assumptions:

$$D_{\mathbf{x}+\boldsymbol{\tau}/2,\mathbf{x}-\boldsymbol{\tau}/2} \approx D_{x,x} + \langle \mathcal{J}_{\mathbf{t}} D_{\mathbf{x}+\mathbf{t}/2,\mathbf{x}-\mathbf{t}/2} \big|_{\mathbf{t}=\mathbf{0}}, \boldsymbol{\tau} \rangle + \boldsymbol{\tau}^\top \mathcal{H}_{\mathbf{t}} D_{\mathbf{x}+\mathbf{t}/2,\mathbf{x}-\mathbf{t}/2} \big|_{\mathbf{t}=\mathbf{0}} \boldsymbol{\tau} \quad (53)$$

$$= \boldsymbol{\tau}^\top \mathcal{H}_{\mathbf{t}} D_{\mathbf{x}+\mathbf{t}/2,\mathbf{x}-\mathbf{t}/2} \big|_{\mathbf{t}=\mathbf{0}} \boldsymbol{\tau} \quad (54)$$

$$= \boldsymbol{\tau}^\top \boldsymbol{\Lambda}_{\mathbf{x}} \boldsymbol{\tau}, \quad (55)$$

$$U_{\mathbf{x}+\boldsymbol{\tau}/2,\mathbf{x}-\boldsymbol{\tau}/2} \approx U_{\mathbf{x},\mathbf{x}} + \langle \mathcal{J}_{\mathbf{t}} U_{\mathbf{x}+\mathbf{t}/2,\mathbf{x}-\mathbf{t}/2} \big|_{\mathbf{t}=\mathbf{0}}, \boldsymbol{\tau} \rangle \quad (56)$$

$$= \langle \mathcal{J}_{\mathbf{t}} U_{\mathbf{x}+\mathbf{t}/2,\mathbf{x}-\mathbf{t}/2} \big|_{\mathbf{t}=\mathbf{0}}, \boldsymbol{\tau} \rangle \quad (57)$$

$$= \langle \boldsymbol{\xi}_{\mathbf{x}}, \boldsymbol{\tau} \rangle. \quad (58)$$

The linearization gives an approximate of kernel values where \mathbf{x} and $\boldsymbol{\tau}$ are separate:

$$k(\mathbf{x} + \boldsymbol{\tau}/2, \mathbf{x} - \boldsymbol{\tau}/2) \approx \sigma_{\mathbf{x}\mathbf{x}} \exp\left(-\frac{1}{2} \boldsymbol{\tau}^\top \boldsymbol{\Lambda}_{\mathbf{x}} \boldsymbol{\tau} + i \langle \boldsymbol{\xi}_{\mathbf{x}}, \boldsymbol{\tau} \rangle\right) \quad (59)$$

$$= \widehat{k}(\mathbf{x} + \boldsymbol{\tau}/2, \mathbf{x} - \boldsymbol{\tau}/2), \quad (60)$$

$$W(\mathbf{x}, \boldsymbol{\omega}) = \int k(\mathbf{x} + \boldsymbol{\tau}/2, \mathbf{x} - \boldsymbol{\tau}/2) e^{-2i\pi \langle \boldsymbol{\omega}, \boldsymbol{\tau} \rangle} d\boldsymbol{\tau} \quad (61)$$

$$\approx \int \widehat{k}(\mathbf{x} + \boldsymbol{\tau}/2, \mathbf{x} - \boldsymbol{\tau}/2) e^{-2i\pi \langle \boldsymbol{\omega}, \boldsymbol{\tau} \rangle} d\boldsymbol{\tau} \quad (62)$$

$$\approx \sigma_{\mathbf{x}\mathbf{x}} \mathcal{N}\left(\boldsymbol{\omega} \middle| \frac{\boldsymbol{\xi}_{\mathbf{x}}}{2\pi}, \frac{\boldsymbol{\Lambda}_{\mathbf{x}}}{2\pi^2}\right) \quad (63)$$

$$= \widehat{W}(\mathbf{x}, \boldsymbol{\omega}), \quad (64)$$

which gives the spectrogram as the approximate Wigner distribution function. The rest of this subsection derives the corresponding $\boldsymbol{\xi}_{\mathbf{x}}$ and $\boldsymbol{\Lambda}_{\mathbf{x}}$ for some GP models.

2.1 The non-stationary quadratic (NSQ) kernel

The NSQ kernel (Paciorek and Schervish, 2004) is a special case of CSK:

$$k_{NS}(\mathbf{x}_i, \mathbf{x}_j) = \frac{|\boldsymbol{\Sigma}_i|^{1/4} |\boldsymbol{\Sigma}_j|^{1/4}}{|(\boldsymbol{\Sigma}_i + \boldsymbol{\Sigma}_j)/2|^{1/2}} e^{-\frac{D_{ij}}{2}}, \quad (65)$$

$$D_{ij} = (\mathbf{x}_i - \mathbf{x}_j)^\top (\boldsymbol{\Sigma}_i + \boldsymbol{\Sigma}_j)^{-1} (\mathbf{x}_i - \mathbf{x}_j), \boldsymbol{\Sigma}_i \succeq \mathbf{0}, \quad (66)$$

$$U_{ij} \equiv 0. \quad (67)$$

It is straightforward that $\boldsymbol{\xi}_{\mathbf{x}} = \mathbf{0}$. Now we derive $\boldsymbol{\Lambda}_{\mathbf{x}}$:

$$\mathcal{H}_{\mathbf{t}} D_{\mathbf{x}+\mathbf{t}/2,\mathbf{x}-\mathbf{t}/2} = \mathcal{H}_{\mathbf{t}} \mathbf{t}^\top (\boldsymbol{\Sigma}_{\mathbf{x}+\mathbf{t}/2} + \boldsymbol{\Sigma}_{\mathbf{x}-\mathbf{t}/2})^{-1} \mathbf{t} \quad (68)$$

$$= (\boldsymbol{\Sigma}_{\mathbf{x}+\mathbf{t}/2} + \boldsymbol{\Sigma}_{\mathbf{x}-\mathbf{t}/2})^{-1}. \quad (69)$$

Other terms involving the Hessian operator are $\mathbf{0}$ because of our assumptions. When $\mathbf{t} = \mathbf{0}$, we get $\boldsymbol{\Lambda}_{\mathbf{x}} = \frac{1}{2} \boldsymbol{\Sigma}_{\mathbf{x}}^{-1}$.

2.2 The generalized spectral mixture (GSM) kernel

The GSM kernel (Remes et al., 2017) augments the NSQ kernel with a cosine term:

$$k_{GSM}(\mathbf{x}_i, \mathbf{x}_j) = k_{NS}(\mathbf{x}_i, \mathbf{x}_j) \exp(iU_{ij}), \quad (70)$$

$$U_{ij} = \langle \boldsymbol{\mu}_i, \mathbf{x}_i \rangle - \langle \boldsymbol{\mu}_j, \mathbf{x}_j \rangle. \quad (71)$$

The lengthscale function conforms to the NSQ kernel: $\boldsymbol{\Lambda}_{\mathbf{x}} = \frac{1}{2}\boldsymbol{\Sigma}_{\mathbf{x}}^{-1}$. The frequencies are derived as:

$$\mathcal{J}_{\mathbf{t}} U_{\mathbf{x}+\mathbf{t}/2, \mathbf{x}-\mathbf{t}/2} \Big|_{\mathbf{t}=\mathbf{0}} = \mathcal{J}_{\mathbf{t}} \left[\boldsymbol{\mu}_{\mathbf{x}+\mathbf{t}/2}^{\top}(\mathbf{x} + \mathbf{t}/2) - \boldsymbol{\mu}_{\mathbf{x}-\mathbf{t}/2}^{\top}(\mathbf{x} - \mathbf{t}/2) \right] \quad (72)$$

$$= \mathcal{J}_{\mathbf{t}} \left[\left(\boldsymbol{\mu}_{\mathbf{x}+\mathbf{t}/2} - \boldsymbol{\mu}_{\mathbf{x}-\mathbf{t}/2} \right)^{\top} \mathbf{x} + \left(\frac{\boldsymbol{\mu}_{\mathbf{x}+\mathbf{t}/2} + \boldsymbol{\mu}_{\mathbf{x}-\mathbf{t}/2}}{2} \right)^{\top} \mathbf{t} \right] \Big|_{\mathbf{t}=\mathbf{0}} \quad (73)$$

$$= \boldsymbol{\mu}_{\mathbf{x}} + (\mathcal{J}_{\mathbf{x}} \boldsymbol{\mu}_{\mathbf{x}}) \mathbf{x}. \quad (74)$$

2.3 The Deep Gaussian process (DGP)

The kernel of DGP is a SE kernel with input warping $\mathbf{f}_i = \mathbf{f}(\mathbf{x}_i)$. Formally,

$$k(\mathbf{x}_i, \mathbf{x}_j) = \exp \left(-\frac{1}{2}(\mathbf{f}_i - \mathbf{f}_j)^{\top} \boldsymbol{\Lambda}(\mathbf{f}_i - \mathbf{f}_j) \right), \quad (75)$$

$$D_{ij} = (\mathbf{f}_i - \mathbf{f}_j)^{\top} \boldsymbol{\Lambda}(\mathbf{f}_i - \mathbf{f}_j). \quad (76)$$

The lengthscale function differ from a constant $\boldsymbol{\Lambda}$ because \mathbf{f}_i is a function of \mathbf{x}_i .

$$\boldsymbol{\Lambda}_{\mathbf{x}} = (\mathcal{J}_{\mathbf{x}} \mathbf{f})^{\top} \boldsymbol{\Lambda} (\mathcal{J}_{\mathbf{x}} \mathbf{f}). \quad (77)$$

3 Inference with covariance function DGPs

3.1 Previous work: maximum *a-posteriori* and Hamiltonian Monte Carlo

Previous work (Paciorek and Schervish, 2004; Heinonen et al., 2016; Remes et al., 2017) have studied inference for the functional hyperparameters of nonparametric kernels. A maximum *a-posteriori* framework gets MAP estimates for values of the hyperparameters on the input points:

$$p(\boldsymbol{\theta}|\mathbf{X}) \propto p(\mathbf{X}, \boldsymbol{\theta}) = p(\mathbf{y}|\mathbf{f})p(\mathbf{f}|\boldsymbol{\theta})p(\boldsymbol{\theta}), \quad (78)$$

Maximizing the posterior likelihood (78), we obtain point estimates for $\boldsymbol{\theta}(\mathbf{X})$.

One point estimate with maximum likelihood does not effectively represent the posterior distribution, the Hamiltonian Monte Carlo (HMC) (Neal, 1993; Heinonen et al., 2016) produces samples from $p(\boldsymbol{\Theta}|\mathbf{X})$ using Hamiltonian dynamics. MAP and HMC are solid choices for small-scale data, but is infeasible in large-scale setting due to the necessity of inferring $O(N)$ parameters.

3.2 Monte Carlo expectation maximization and the SG-HMC sampler

For hyperparameter learning using SG-HMC, we use the moving window Monte Carlo expectation maximization (MCEM) (Havasi et al., 2018), an extension of the expectation maximization algorithm to learn maximum likelihood estimate of hyperparameters. The moving window MCEM keeps track of a fixed-length window of recent samples from HMC sampler, and each optimization action of hyperparameters is done given the parameters randomly drawn from the window. This algorithm has shown better optimization of hyperparameter for deep GP models (Havasi et al., 2018).

In practice, we use the auto-tuning approach given by (Springenberg et al., 2016), which has shown to work well for Bayesian neural networks, as well as compositional DGPs (Havasi et al., 2018).

3.3 Doubly stochastic variational inference: a derivation

Salimbeni and Deisenroth (2017b) proposes a DS-VI framework for DGPs with NSQ covariance with omitted derivation. Here we provide a detailed derivation. The main idea is to approximate the evidence lower bound with Monte Carlo samples. We first consider variational distributions that factorize over f and θ : $q(\mathbf{u}_f, \mathbf{u}_\theta) = \mathcal{N}(\mathbf{u}_f | \mathbf{m}_f, \mathbf{S}_f) \mathcal{N}(\mathbf{u}_\theta | \mathbf{m}_\theta, \mathbf{S}_\theta)$. we can thus get the approximated posterior:

$$q(\mathbf{f}, \theta, \mathbf{u}_f, \mathbf{u}_\theta) = p(\mathbf{f} | \mathbf{u}_f, \theta) q(\mathbf{u}_f) p(\theta | \mathbf{u}_\theta) q(\mathbf{u}_\theta). \quad (79)$$

Here we can employ a Monte Carlo sampling of $\hat{\theta}$. A stochastic estimate of ELBO can be obtained:

$$\mathcal{L}_{\text{CSK}} = \log p(\mathbf{y} | \hat{\mathbf{f}}) - \text{KL}(q(\mathbf{u}_f) || p(\mathbf{u}_f | \hat{\theta})) - \text{KL}(q(\mathbf{u}_\theta) || p(\theta)). \quad (80)$$

Empirically, we use a whitened representation of the variational parameter: $\check{\mathbf{u}}_\theta = k_\theta(\mathbf{Z}_\theta, \mathbf{Z}_\theta)^{-1/2} \mathbf{u}_\theta$.

4 Experiment details

Our experiments mainly include the following models: the sparse Gaussian process regression (Titsias, 2009), the sparse variational Gaussian process (Hensman et al., 2013), the doubly stochastic variational deep Gaussian process (Salimbeni and Deisenroth, 2017a) and the proposed stochastic gradient Hamiltonian Monte Carlo method for inferring covariance function DGPs.

4.1 Solar irradiance

With the solar irradiance dataset (Lean, 2004)², we follow the same partition of training and test set as Gal and Turner (2015) and Hensman et al. (2017). This 1-dimensional dataset has 281 training points and 110 test points. We standardize both \mathbf{X} and \mathbf{Y} before the regression.

We use 3 components to fit the SM kernel as well as CSK. The HMK kernel has 6 centroids, each with three frequency terms. We initialize all parameters (including kernel hyperparameters for parametric kernels, kernel hyperparameters for latent GPs of NSQ and CSK, variational parameters, inducing points, and parameters sampled from HMC) at random. And we do 5000 iterations for each models, with a learning rate of 10^{-3} .

4.2 New York Yellow Taxi dataset

Due to limited time and CSK’s sensitivity to higher dimensions, we use a subset of the New York Taxi dataset³, subsampling 25% of all taxi trips from the first two months (Jan-Feb 2016). The dataset has 5 dimensions (longitudes and latitudes of the pickup and dropoff locations, and the date and time of the beginning of the taxi trip). We combine the date and time to a “date value”. The training set includes 100671 data points, and the test set includes 45260 data points. We also standardize both input and output before regression.

We use minibatch of 10000 given the medium-large scale of data. We use the stochastic variational GP (Hensman et al., 2013) for GPs with parametric kernels (SE kernel and SM kernel), and SG-HMC (Havasi et al., 2018) for compositional DGP, and the proposed SG-HMC for GP with NSQ kernel and CSK. For CSK and SM, we use 4 frequency components. The parameters are again initialized at random, except for the inducing points randomly initialized with a K-Means algorithm.

²https://github.com/jameshensman/VFF/blob/master/experiments/solar/solar_data.txt

³<https://www.kaggle.com/c/nyc-taxi-trip-duration/overview>